Electrochemical Synthesis and Investigation of Stoichiometric, Phase Pure $CoSb_2O_6$ and $MnSb_2O_6$ Electrodes for the Oxygen Evolution Reaction in Acidic Media

Taylor A. Evans and Kyoung-Shin Choi*

Department of Chemistry, University of Wisconsin-Madison, Madison, WI 53706.

*Corresponding author. Email: kschoi@chem.wisc.edu

ABSTRACT

The electrochemical oxidation of water to oxygen gas is the primary counter reaction to the formation of hydrogen gas via water splitting. In acidic media, the only well-established and active oxygen evolution catalysts are expensive noble metal oxides such as IrO_x and RuO_x, necessitating the development of practical oxygen evolution catalysts that are stable in acidic media. In this study, we prepared stoichiometric, phase pure $CoSb_2O_6$ and $MnSb_2O_6$ electrodes using electrochemical synthesis and investigated their ability to oxidize water in 0.5 M H_2SO_4 (pH 0.3). In addition, their stabilities during the oxygen evolution reaction (OER) were carefully examined by comparing their morphologies, crystallinities, compositions, and surface compositions before and after the OER. The chlorine evolution reaction on $CoSb_2O_6$ and $MnSb_2O_6$ in acidic media was also examined so that their performances can be compared with previously reported non-stoichiometric $CoSb_2O_6$ and $MnSb_2O_6$ electrodes. The electrochemical properties and stabilities of stoichiometric, phase pure $CoSb_2O_6$ and $MnSb_2O_6$ reported in this study can provide useful insights for the development and understanding of acid-stable, non-noble metal oxide-based OER catalysts.

INTRODUCTION

Electrochemical water splitting using electricity generated by renewable sources offers an environmentally benign and sustainable route for H_2 production.[1-3] The electrical energy required for water splitting is determined not only by the thermodynamic potential requirement for water splitting but also by the kinetic overpotential requirements for the hydrogen evolution reaction (HER) and oxygen evolution reaction (OER). Thus, a significant effort has been made for the development of efficient, stable, and inexpensive catalysts for the HER and OER. Oxygen evolution catalysts (OECs), in particular, have been intensively investigated as the OER typically requires more overpotential due to its kinetically more complex four-electron process.[4,5]

While metal-oxide OECs for use in alkaline media have been well established with regards to high performance, long lasting stability, and low cost,[6,7] the progress in the development of practical OECs that work in acidic media has been slow. This is because not many elements or compounds are stable in acidic media (pH < 1) and under the strongly anodic conditions (> 1.2 V vs. RHE) required for the OER. As a result, the only well-established materials that are able to perform the OER in acidic media are expensive noble metal oxides, namely IrO_x and RuO_x.[8-10] However, even these materials are not stable over extended periods of time.[11-13] Considering that proton exchange membrane (PEM) electrolyzers that operate in acidic media have distinctive advantages over alkaline electrolyzers, which include higher current densities and low gas crossover,[14] the development of inexpensive and stable OECs for use in acidic media is of great interest.

In order to develop OECs for acidic media, phases that can be stable in acidic media and under anodic biases need to be identified first. According to Pourbaix diagrams, Sb_2O_5 is one of the few oxides that are thermodynamically stable in acidic media and under anodic biases.[15] However, Sb_2O_5 is a wide bandgap insulator with overall poor conductivity.[16-18] Furthermore, Sb_2O_5 itself has never been shown to

have catalytic activity for any electrochemical oxidation reactions. Thus, we turn to Sb^{5+}-based ternary oxides, whereby the stability of an antimony oxide matrix in acid may be combined with first-row transition metals that are well known for their catalytic activity for the OER to form acid-stable OECs.

Recent work has reported that Sb-containing oxides with a formula of MSb_2O_6 (M = Mn, Ni, and Co) that have a rutile structure can perform the OER in acidic media.[19-21] For example, Moreno-Hernandez *et al.* reported that $Ni_{2-x}Mn_xSb_{1.6-1.8}O_y$ prepared by sputter coating can perform the OER in 1 M H_2SO_4.[19] However, the authors reported severe losses of the constituent metal ions by dissolution after a prolonged stability test. For example, $Ni_{0.5}Mn_{0.5}Sb_{1.7}O_y$ lost more than 50% of Mn by dissolution during a stability test performed at 10 mA/cm^2 for 150 h.

We note that the compounds used in this study did not have the stoichiometric M:Sb ratio (1:2). Instead, they were M-rich or Sb-poor compounds (i.e. $MnSb_{1.6}O_x$ and $Ni_{0.5}Mn_{0.5}Sb_{1.6}O_x$). In this case, it is not clear whether the observed OER performance and the dissolution loss of the compounds during the OER are the intrinsic properties of pure MSb_2O_6 phases or whether they are due to the presence of a defective Mn-rich phase formed on the surface of MSb_2O_6. In fact, a study by Zhou *et al.,* which prepared a library of a Mn-Sb-O system with varying Mn:Sb ratios using physical vapor deposition reported that phases with higher Mn content (i.e. Mn/Sb = 1) showed higher current densities for the OER but they lost more Mn by dissolution during the OER.[20] Zhou *et al.* also reported that enhanced OER activity of the Mn-rich phase is due to the increased presence of Mn^{3+} centers. Considering that Mn^{3+}-containing amorphous binary oxides or hydroxides are known to be catalytic for the OER,[22,23] but not stable in strongly acidic media (pH < 2), it is possible that the OER performance and stability of Mn-rich $MnSb_2O_6$ reported in the previous studies may not be mainly governed by $MnSb_2O_6$ but by Mn^{3+}-rich defected phases or Mn^{3+}-containing amorphous binary phases at the surface.

In a more recent study, Moreno-Hernandez *et al.* compared the activity of $CoSb_2O_6$ and $MnSb_2O_6$ for water oxidation and chloride oxidation in acidic media and reported that $CoSb_2O_6$ is more active for

chloride oxidation than $MnSb_2O_6$.[21] We note that the $CoSb_2O_6$ used in this study was slightly Sb-rich ($CoSb_{2.2}O_x$) while the $MnSb_2O_6$ used in this study was Mn-rich ($MnSb_{1.7}O_x$). In this case, we are curious whether the observed performance difference is solely caused by the difference in the type of transition metal (Co vs. Mn) or by the type of non-stoichiometry (i.e. M-rich vs. Sb-rich) present in these compounds.

The purpose of the current study is to prepare stoichiometric, phase pure $CoSb_2O_6$ and $MnSb_2O_6$ to examine their activity and stability for the OER in a strongly acidic medium, which will greatly complement the results obtained from previous investigations and increase our general understanding of the properties of MSb_2O_6 compounds. To achieve this goal, we developed new electrodeposition methods to prepare highly uniform, nanocrystalline $CoSb_2O_6$ and $MnSb_2O_6$ electrodes. After examining the OER performances and stabilities of these compounds, we additionally examined their performance for the chloride oxidation reaction, so that a more comprehensive understanding of these systems for electrochemical oxidation reactions in acidic media can be obtained.

EXPERIMENTAL

Materials. Cobalt chloride ($CoCl_2 \cdot 6H_2O$, 98%), manganese chloride ($MnCl_2 \cdot 4H_2O$, >99%), potassium antimony tartrate ($K_2Sb_2(C_4H_2O_6)_2 \cdot H_2O$, 99%), TraceCERT antimony ICP standard, TraceCERT manganese ICP standard, TraceCERT cobalt ICP standard, and sulfuric acid (H_2SO_4, 95-98%) were purchased from Sigma-Aldrich, and potassium nitrate (KNO_3, 99%) was purchased from Alfa Aesar. All chemicals were used without further purification after purchase. Fluorine doped tin oxide (FTO) on borosilicate glass (Solaronix) was used as the working electrode for electrodeposition. The platinum counter electrode was prepared by depositing 20 nm of titanium as an adhesion layer, followed

by 100 nm of platinum on clean glass slides via e-beam evaporation. All solutions were prepared using deionized (DI) water with a resistivity of 18.2 MΩ·cm. FTO substrates were cleaned before deposition by gently rubbing the surface with soap and water followed by sonication in isopropyl alcohol, acetone, and then twice in water, with each solvent step taking 15 minutes, then being dried under a stream of air.

Synthesis of $CoSb_2O_6$ and $MnSb_2O_6$. In order to prepare $CoSb_2O_6$, a film composed of $Co(OH)_2$ and Sb was first electrodeposited as the precursor film. Electrodeposition was carried out using a VMP2 multichannel potentiostat (Princeton Applied Research) in an undivided 3 electrode cell composed of a FTO working electrode, a Ag/AgCl (4 M KCl) reference electrode and a Pt counter electrode. The FTO electrode was masked off to a geometric surface area of 0.5 cm^2 with insulating tape (3M, electroplating tape 470).[24] This had the outcome of removing edge effects and improving the uniformity of the film. An aqueous solution containing 43 mM $CoCl_2 \cdot 6H_2O$, 11.5 mM $K_2Sb_2(C_4H_2O_6)_2 \cdot H_2O$, and 400 mM KNO_3 was used as the plating solution. The precursor film was deposited at -1.35 V vs Ag/AgCl by passing 0.4 C/cm^2. In order to prepare $MnSb_2O_6$, a film composed of $Mn(OH)_2$ and Sb was electrodeposited as the precursor film. In this case, the plating solution contained 26 mM $MnCl_2 \cdot 4H_2O$, 11 mM $K_2Sb_2(C_4H_2O_6)_2 \cdot H_2O$, and 800 mM KNO_3. The precursor film was deposited at -1.35 V vs Ag/AgCl by passing 0.04 C/cm^2. The as-deposited amorphous precursor films were converted to crystalline $CoSb_2O_6$ and $MnSb_2O_6$ by annealing at 700 °C for 3 hours in air (ramping rate = 1.9 °C/min). After the three hours of anneal time, the films were left to cool down to room temperature for approximately three hours within the furnace.

Characterization. The sole presence of the AB_2O_6 crystalline phase was confirmed via powder X-ray diffraction (PXRD, D8 Discover, Bruker, Ni-filtered Cu Kα radiation, λ = 1.5418 Å). The surface morphology and elemental composition of the electrodes was characterized with scanning electron microscopy (SEM; LEO Supra55 VP) and energy dispersive spectroscopy (EDS; Noran System Seven, Thermo-Fisher, ultra-dry silicon drift detector) using an accelerating voltage of 2 keV for SEM and 20

keV for EDS. The elemental ratios were calculated using the Thermo Scientific NSS software package (Filter without Standards Quant Fit method and the Proza correction method). Since the Lα signal of Sn (3.443 keV) from the FTO substrate partially overlaps with the Lα signal of Sb (3.604 keV) from the samples preventing accurate quantification of the sample compositions, powder samples obtained by scrapping the as-deposited films off the FTO substrate were attached to carbon tape and used for EDS analysis. The elemental analyses of the samples were also performed using inductively coupled plasma mass spectrometry (ICP-MS) (Shimadzu ICP Mass Spectrometer-2030) using the solutions obtained by dissolving the as-deposited films in 0.5 M H_2SO_4. Calibration curves were created using the cobalt, manganese and antimony ICP standards diluted with 0.5 M H_2SO_4. ICP-MS was also used to quantify metal ions dissolved in the electrolyte during a 24 V-t measurement to evaluate the electrochemical stability of the samples. Surface elemental compositions were determined with X-ray photoelectron spectroscopy (XPS) using a Thermo Scientific K-α X-ray photoelectron spectrometer equipped with an Al Kα excitation source. The peak binding energies were calibrated to the adventitious C_{1s} peak at 284.8 eV. The surface elemental ratios were calculated using the Thermo Avantage Software package (ALThermo1 library for sensitivity factors, TPP-2m IMFF for energy correction, and a modified Shirley background for background correction).

Electrochemical characterization. Electrochemical measurements were performed using either a VMP2 multichannel potentiostat (Princeton Applied Research) or an SP-200 potentiostat/EIS (Bio-Logic Science Instrument). The working electrode of either $CoSb_2O_6$ or $MnSb_2O_6$, was masked with epoxy (Devcon) to a working geometric surface area of ~0.15 cm^2. An undivided three-electrode cell containing a working electrode of either $CoSb_2O_6$ or $MnSb_2O_6$, a Ag/AgCl (4 M KCl) reference electrode, and a Pt counter electrode was used for characterization unless otherwise noted.

Linear sweep voltammetry's (LSVs) were performed at a scan rate of 10 mV/s by sweeping the potential in the positive direction from the open circuit potential. All LSVs shown in this study were

corrected for the uncompensated solution resistance (R_u) after each experiment, which ranged from 2 and 5 Ohms. The R_u was determined by electrochemical impedance spectroscopy (EIS) where impedance was measured at 1.85 V vs RHE with a frequency range of 100 kHz to 1 Hz and a sinusoidal amplitude of 10 mV with a planar Pt electrode.[19,25,26] The electrochemically active surface area (ECSA) of $CoSb_2O_6$ or $MnSb_2O_6$ electrodes was estimated using the impedance of each electrode obtained under the aforementioned conditions by fitting with a modified Randles circuit composed of a parallel combination of a resistor and a constant phase element in series with a resistor (**Figure S1**).[25] Galvanostatic water oxidation was performed at 10 mA/cm^2. All electrochemical experiments were performed in 0.5 M H_2SO_4 (pH 0.3) unless otherwise noted and without agitation (except for the galvanostatic water oxidation experiments where stirring was used to assist in removal of bubbles forming on the electrode surface).

The Faradaic efficiency (FE) for O_2 evolution was determined using a custom designed, air tight, two compartment, glass cell with a smaller Ag/AgCl (3 M NaCl) reference electrode. O_2 gas generated was detected using an Ocean Optics fluorescence-based oxygen sensor (Neofox FOSPOR-R). The oxygen sensor measured the O_2 content in the headspace as mole %. This was converted to μmol after first adjusting for the O_2 dissolved in solution using Henry's Law. The overall FE for O_2 evolution was calculated by the following equation:

$$\text{FE (\%)} = \frac{4 \text{ x } n_{O_2}\text{(mol) x F (C mol}^{-1}\text{)}}{\text{Total charged passed (C)}} \text{ x } 100$$

While a Ag/AgCl reference was used in each experiment performed, all results within this report are presented against the reversible hydrogen electrode (RHE) for direct comparison to other reports in aqueous solution but that contain different pH values. The conversion between Ag/AgCl and RHE reference electrode values can be done via the following equation:

$$E_{(\text{vs RHE})} = E_{(\text{vs Ag/AgCl})} + E_{(\text{Ag/AgCl})}\text{(reference)} + 0.0591 \text{ V x pH(at 25 °C)}$$

$E_{Ag/AgCl}$(reference, 4 M KCl) = 0.1976 V vs NHE at 25 °C

$E_{Ag/AgCl}$(reference, 3 M NaCl) = 0.209 V vs NHE at 25 °C

RESULTS AND DISCUSSION

Synthesis, Characterization, and OER performance of $CoSb_2O_6$ and $MnSb_2O_6$. The $CoSb_2O_6$ electrodes used for this study were synthesized via an electrochemical co-deposition of cobalt hydroxide and antimony metal using a plating solution composed of potassium antimony tartrate, cobalt chloride, and potassium nitrate. The Co was co-deposited not as Co metal but as $Co(OH)_2$ because the reduction potential of Co^{2+} to Co^0 is more negative than that of Sb^{3+} to Sb^0.[15] Under the potential used to deposit Sb, nitrate is reduced to nitrite as shown by the equation below:[27]

$$NO_3^- + H_2O + 2e^- \rightleftharpoons NO_2^- + 2OH^-$$

The OH^- produced by this reaction increases the local pH at the WE surface, decreasing the solubility of Co^{2+}, and results in the precipitation of Co^{2+} as $Co(OH)_2$. The deposition potential and the Co:Sb ratio in the plating solution were adjusted such that the Co:Sb ratio in the as-deposited film is exactly and uniformly 1:2 throughout the films, which was confirmed by energy dispersive X-ray spectroscopy (EDS). The bulk Co:Sb ratio of the as-deposited film was additionally confirmed to be 1:2 using inductively coupled plasma mass spectrometry (ICP-MS) of the solution obtained by the dissolution of the entire as-deposited film in 0.5 M H_2SO_4. The $MnSb_2O_6$ electrodes were prepared in the same manner but with replacement of the cobalt chloride with manganese chloride. Both the EDS and ICP-MS results confirmed that the Mn:Sb ratio in the as-deposited film is 1:2. The X-ray diffraction (XRD) patterns of the as-deposited films show that both films are amorphous (**Figure S2**).

The as-deposited films were converted to crystalline $CoSb_2O_6$ and $MnSb_2O_6$ by annealing in air for three hours at 700 °C (**Figure 1**). The SEM images show the uniform nanocrystalline nature of the $CoSb_2O_6$ and $MnSb_2O_6$ films (**Figure 2**). Using EDS the Co:Sb and Mn:Sb ratios were confirmed to remain as 1:2 after annealing. The side view SEM images (**Figure S3**) show that the thickness of the $CoSb_2O_6$ and $MnSb_2O_6$ are ~600 nm and ~200 nm, respectively. Any attempt to grow a thicker film resulted in the formation of films with less uniform Co(or Mn):Sb ratios throughout the films. The XRD pattern of $CoSb_2O_6$ clearly shows the formation of a crystalline $CoSb_2O_6$ phase with a rutile structure. However, the crystalline phase of $MnSb_2O_6$ could not be confirmed by XRD due to two reasons. First, since the $MnSb_2O_6$ film is extremely thin and nanocrystalline, the peak intensities were very low compared with those from the FTO substrate. Second, since both the FTO and $MnSb_2O_6$ have the same rutile structure with similar cell parameters, the peaks from $MnSb_2O_6$ overlap closely with those from the FTO substrate. Thus, in order to confirm the structure type of $MnSb_2O_6$, we grew a thicker $MnSb_2O_6$ film on a non-rutile phase substrate (i.e. indium tin oxide (ITO)). Compared with the ~200 nm thin film, the stoichiometry of this thicker $MnSb_2O_6$ film was not as uniform throughout the film. However, its XRD shows peaks only from $MnSb_2O_6$ and confirmed that $MnSb_2O_6$ produced using our new method has a rutile structure (**Figure S4**).

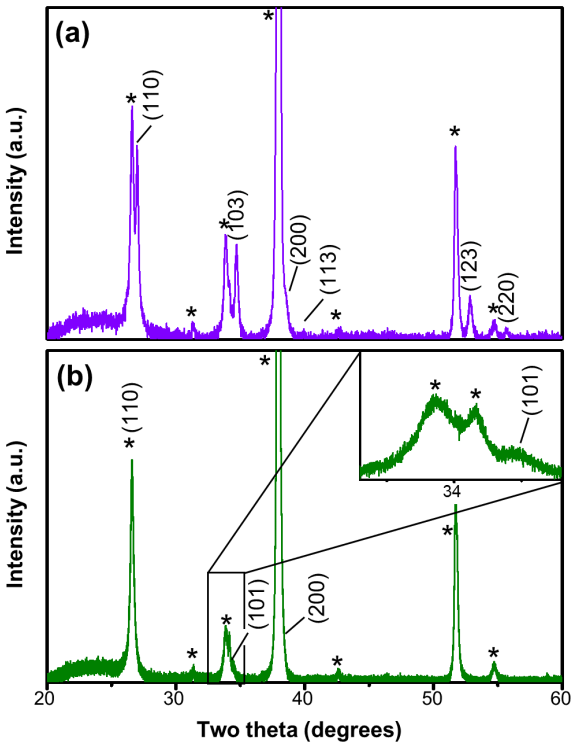

Figure 1. XRD patterns of annealed (a) $CoSb_2O_6$ (purple) and (b) $MnSb_2O_6$ (green) with an inset for $MnSb_2O_6$ to aid in showing the appearance of peaks after annealing. The (*hkl*) indices are assigned from the PDF cards for $CoSb_2O_6$ (00-018-0403) and $MnSb_2O_6$ (04-011-4962). The peaks corresponding to the FTO substrate are denoted by an asterisk.

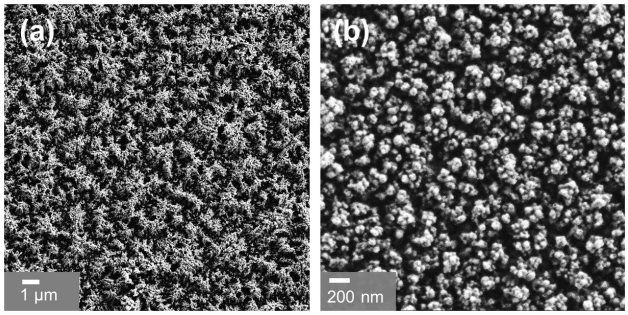

Figure 2. Top-view SEM images of (a) $CoSb_2O_6$ and (b) $MnSb_2O_6$ electrodes obtained after annealing.

The water oxidation performance of $CoSb_2O_6$ and $MnSb_2O_6$ electrodes was investigated using linear sweep voltammetry (LSV) in 0.5 M H_2SO_4 (pH 0.3) (**Figure 3a**). In order to show the unambiguous

effect of incorporating Co^{2+} and Mn^{2+} into the Sb oxide matrix on the OER performance, the LSV of Sb_2O_4 ($Sb^{3+}Sb^{5+}O_4$) is also shown for comparison. Sb_2O_4 is the oxide that is obtained when antimony metal electrodeposited on FTO alone is annealed in the air using the same conditions to obtain crystalline $CoSb_2O_6$ and $MnSb_2O_6$ electrodes.

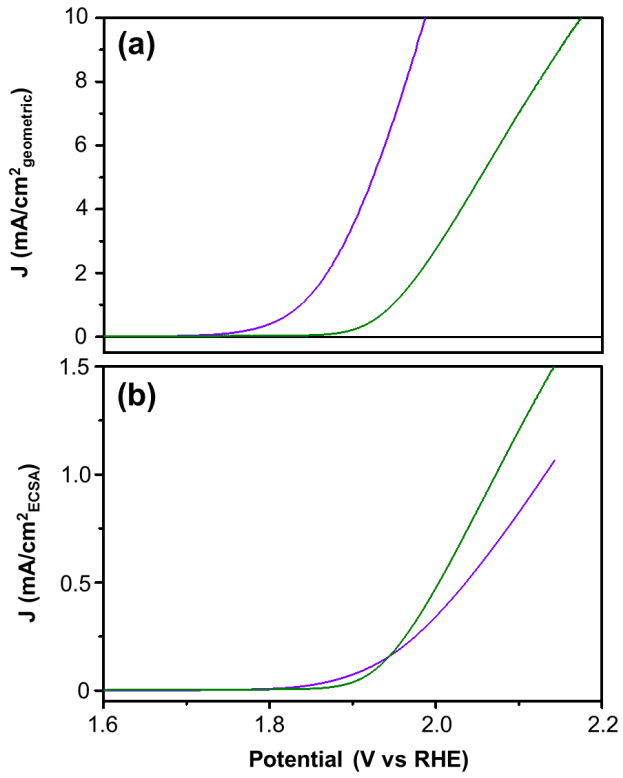

Figure 3. (a) LSVs of $CoSb_2O_6$ (purple), $MnSb_2O_6$ (green), and Sb_2O_4 (black) in 0.5 M H_2SO_4 (pH 0.3) with the current density determined using the geometric surface area of the electrode. (b) LSVs of $CoSb_2O_6$ (purple) and $MnSb_2O_6$ (green) with the current density determined using the electrochemically active surface areas.

The LSV of Sb_2O_4 shows no anodic current when the potential was swept to 2.2 V vs. RHE, suggesting that it is inactive for the OER. On the other hand, $CoSb_2O_6$ and $MnSb_2O_6$ generated considerable anodic currents due to the OER, suggesting that their OER activity truly originates from the presence of Co and Mn in the compounds. The overpotential required to achieve 10 mA/cm^2 was ~0.760

V for $CoSb_2O_6$ and ~0.940 V for $MnSb_2O_6$. (Extended LSVs showing the current densities reaching 100 mA/cm^2 can be found in **Figure S5**.) Using these values alone, $CoSb_2O_6$ appeared to be more active for the OER. However, we note that the $CoSb_2O_6$ film used in this study was ~3 times thicker than the $MnSb_2O_6$ film, meaning that the surface area of the $CoSb_2O_6$ electrode is significantly higher than that of $MnSb_2O_6$ electrode (**Figure S2**). This is because the thickness of the $CoSb_2O_6$ and $MnSb_2O_6$ electrodes used in this study was individually optimized to obtain the purest composition for each sample. To eliminate the effect caused by the difference in surface area of these films, the electrochemically active surface area (ECSA) of the electrodes was determined using electrochemical impedance spectroscopy (EIS).

Our result showed that the roughness factors of the $CoSb_2O_6$ and $MnSb_2O_6$ electrodes were ~18 and ~6, respectively. Using these values, the current densities were recalculated and LSVs were re-plotted in **Figure 3b**. The ECSA-adjusted LSVs show that although $CoSb_2O_6$ has a slightly earlier onset, $MnSb_2O_6$ shows a greater rise in current density as the potential is swept more positively, indicating that $MnSb_2O_6$ is intrinsically more active for the OER in the potential region to generate a sufficient amount of current. However, our data also suggests that the difference in their intrinsic performance is not significant and a higher current density towards the OER can be achieved by $CoSb_2O_6$ when it is prepared as a higher surface area electrode (**Figure 3a**).

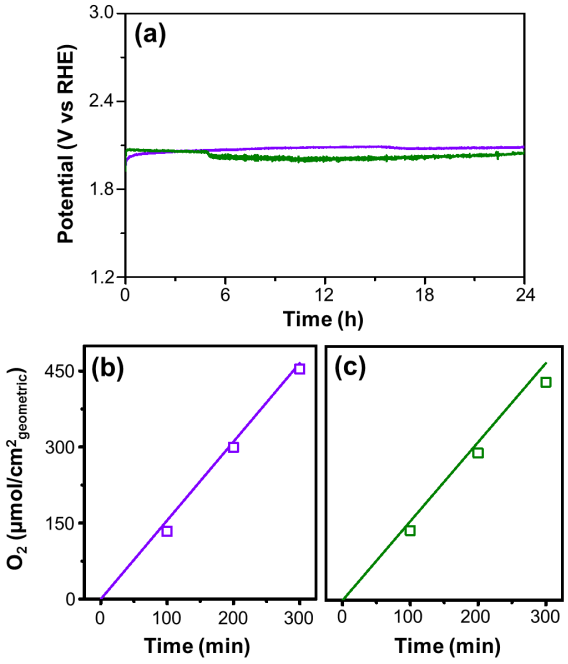

Figure 4. (a) V-t plots of $CoSb_2O_6$ (purple) and $MnSb_2O_6$ (green) obtained for galvanostatic water oxidation at 10 mA/cm^2 in 0.5 M H_2SO_4 (pH 0.3). Oxygen produced by (b) $CoSb_2O_6$ and (c) $MnSb_2O_6$ electrodes during galvanostatic water oxidation at 10 mA/cm^2 in 0.5 M H_2SO_4 (pH 0.3) (open squares). The theoretically expected amount of oxygen, assuming 100% FE, is shown as a solid line.

The stability of $CoSb_2O_6$ and $MnSb_2O_6$ during the OER in acidic media was first examined under galvanostatic water oxidation at 10 mA/cm$^2_{geometric}$ by recording the change in the potential required to maintain this current density over 24 h (**Figure 4a).** The result shows negligible change in the required potential for both compounds. We confirmed that the current generated during this experiment was truly associated with O_2 production by calculating the Faradic efficiency (FE) for O_2 production by comparing the amount of O_2 detected and the amount of O_2 theoretically calculated assuming 100 % FE (**Figure 4b,c**). The FEs for O_2 production of both compounds were greater than or equal to 95% (98% for $CoSb_2O_6$ and 95% for $MnSb_2O_6$ at 300 min). However, we note that the overpotentials required to achieve 10 mA/cm^2 by $CoSb_2O_6$ and $MnSb_2O_6$ are significantly higher than that of state-of-the-art catalysts in acidic or basic conditions.[25,28]

Post OER Analysis. Although the V-t plots suggested the stability of these compounds during the OER, the work by Moreno-Hernandez *et al.* clearly demonstrated that stable V-t performance does not necessarily mean that the catalyst is stable. Their sample, $Ni_{0.5}Mn_{0.5}Sb_{1.7}O_y$, lost more than 50% of its Mn by dissolution during the V-t measurement but this severe corrosion did not affect the required potential to generate 10 mA/cm^2 over 150 h.[19] Thus, we performed careful post analysis of the films using various techniques after the 24 h V-t measurement at 10 mA/cm^2 to examine for any possible signs of corrosion.

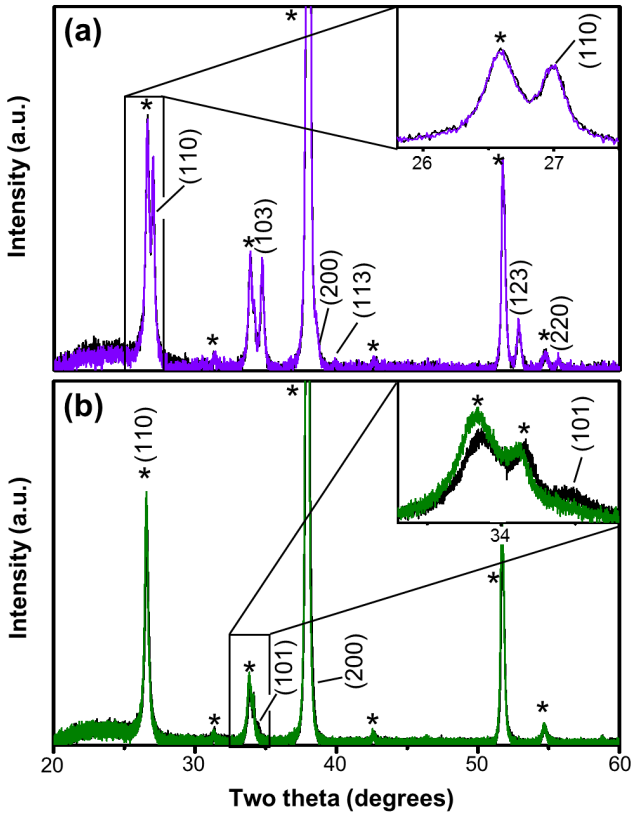

Figure 5. XRD patterns of (a) $CoSb_2O_6$ and (b) $MnSb_2O_6$ electrodes after a 24 h V-t measurement at 10 mA/cm^2. XRD patterns of the corresponding films before the V-t measurement are shown in black for comparison. The peaks corresponding to the FTO substrate are denoted by an asterisk.

Figure 5 shows the XRD patterns before and after the V-t measurement, with insets showing the intensity changes of the most representative and intense peak for both compounds. The (110) peak of $CoSb_2O_6$ showed no difference in intensity before and after the V-t measurement. However, the (101)

peak of $MnSb_2O_6$ showed a decrease in intensity, indicating possible loss of $MnSb_2O_6$ during the V-t measurement. SEM images of these electrodes taken after the V-t measurement (**Figure 6**) agree well with the XRD patterns; no noticeable morphological changes were observed for $CoSb_2O_6$, however, for $MnSb_2O_6$ the void space between the nanoparticles became larger due to the pitting caused by the loss of $MnSb_2O_6$ by dissolution. The EDS analysis of $MnSb_2O_6$ showed that the Mn:Sb ratio remained 1:2, suggesting that the corrosion involved the dissolution of both Mn and Sb and not the preferential leaching of Mn or Sb.

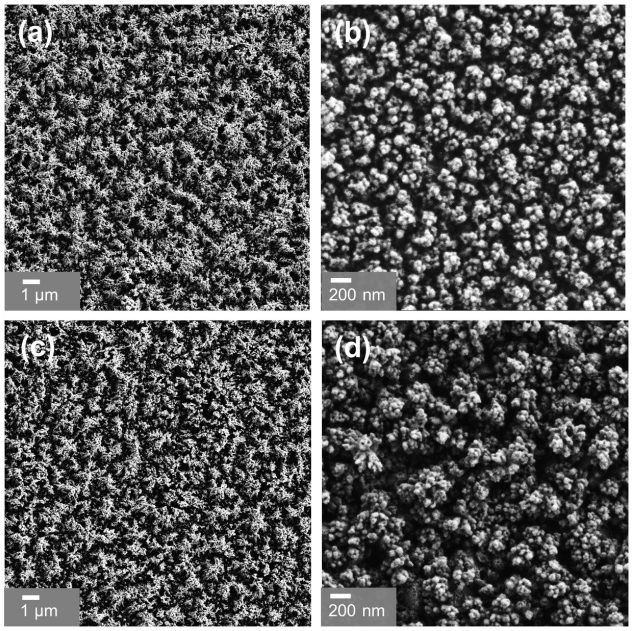

Figure 6. Top-view SEM images of (a,c) $CoSb_2O_6$ and (b,d) $MnSb_2O_6$ electrodes before (top) and after (bottom) the galvanostatic water oxidation at 10 mA/cm^2 for 24 h.

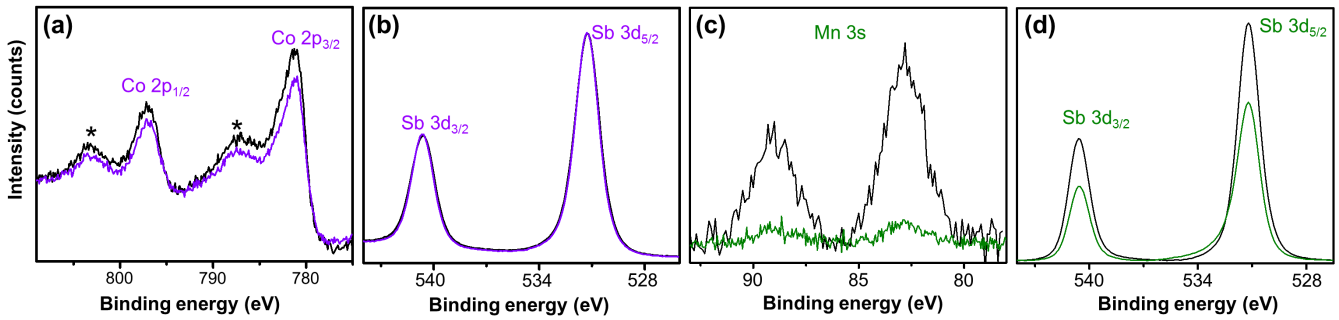

Figure 7. XPS of (a) Co 2p and (b) Sb 3d regions of $CoSb_2O_6$ and (c) Mn 3s and (d) Sb 3d regions of $MnSb_2O_6$ before (black) and after (colored) the V-t measurement at 10 mA/cm^2 for 24 h. The asterisks in the Co 2p spectra denote satellite peaks.

We also performed X-ray photoelectron spectroscopy (XPS) before and after the V-t measurement to probe for changes in the oxidation states of the constituent elements on the $CoSb_2O_6$ and $MnSb_2O_6$ electrode surfaces. The Co 2p region of $CoSb_2O_6$ is shown in **Figure 7a** and is composed of $2p_{2/3}$, $2p_{1/2}$, and their satellite peaks. We used the $2p_{1/2}$ peak to examine the oxidation state of Co in $CoSb_2O_6$ because the position of the $2p_{1/2}$ peak moves more drastically with changes in oxidation state than that of the $2p_{3/2}$ peak.[29,30] For an oxide containing only Co^{2+} the $2p_{1/2}$ peak is expected to appear at 796.6 eV, with a satellite feature at 802.3 eV, while one containing only Co^{3+} will have the $2p_{1/2}$ peak at 794.8 eV with a satellite feature at 804.3 eV. For our pristine $CoSb_2O_6$ electrode the $2p_{1/2}$ peak was centered at 796.7 eV and the satellite peak at 802.8 eV, indicating the presence of Co^{2+} at the surface, which is also the oxidation state of Co in the bulk $CoSb_2O_6$.[29,30] **Figure 7a** also shows that the peak positions did not change after the V-t measurement, indicating that the oxidation state of Co at the surface is still +2. However, a small decrease in the Co 2p region intensity occurred, indicating a small decrease in the relative amount of Co on the surface compared to Sb. The surface Co:Sb ratio before the V-t measurement was 1:2.07, very close to the bulk elemental ratio of 1:2. After the V-t measurement, the surface Co:Sb ratio was 1:2.29 suggesting a slight loss of Co from the outer most surface layer. We note that this surface Co:Sb ratio is still close to the bulk Co:Sb ratio of $CoSb_2O_6$. For comparison, the Co:Sb ratios of the Sb-rich $CoSb_2O_6$ prepared by Moreno-Hernandez *et al*. were 1:4.0 and 1:4.5 before and after the V-t measurements, respectively.[21]

The Sb 3d region of $CoSb_2O_6$ is shown in **Figure 7b.** The $3d_{5/2}$ peak in this plot overlaps with the O 1s peak.[31,32] Thus, the Sb $3d_{3/2}$ peak was used to examine the oxidation state of Sb on the $CoSb_2O_6$ surface. For the Sb $3d_{3/2}$ peak, Sb^{3+} oxides show a peak at a binding energy of 539.6 eV, Sb^{5+} oxides at 540.6 eV, and an even mixture ($Sb^{3+}Sb^{5+}O_4$) at a binding energy in-between at 540.0 eV. The Sb $3d_{3/2}$

peak of the pristine $CoSb_2O_6$ electrode is centered at 540.5 eV, which indicates a surface that is primarily Sb^{5+} in nature.[31,32] After the 24 hour V-t measurement, the Sb $3d_{3/2}$ peak shifted to 540.6 eV, indicating an increase of Sb^{5+} character to that of the pure Sb^{5+} oxide phase. We note that the as-prepared Sb-rich $CoSb_{2.2}O_6$ prepared by Moreno-Hernandez *et al* showed the Sb $3d_{3/2}$ peak at 539.7 eV, meaning that it contains a considerable amount of Sb^{3+} on the surface compared with our stoichiometric $CoSb_2O_6$.[21]

Figure 7c shows the Mn 3s region of the $MnSb_2O_6$ electrode containing the doublet associated with the 3s electrons. The splitting of the Mn 3s peak into a doublet arises from the coupling between the non-ionized 3s electrons and the valence electrons in the 3d orbitals.[33] This splitting provides a useful way to examine the Mn oxidation state, as the distance between the two peaks can provide information on the surface oxidation state, where higher oxidation states show a smaller binding energy difference and lower oxidation states show a larger binding energy difference. The trend of increasing oxidation state leading to a decrease in the distance between the two peaks is agreed upon and a range of values for each oxidation state can be found within the literature. For MnO the distance between the two peaks is reported between 5.7-6.3 eV, for Mn_2O_3 it is 5.2-5.4 eV and for MnO_2 it is 4.5-4.7 eV.[33-37] For the pristine $MnSb_2O_6$, we observe the Mn 3s splitting to be 6.1 eV, which lies firmly within the range of differences in binding energies associated with Mn^{2+}. After the 24 hour V-t measurement, we see a significant decrease in the Mn 3s signal, as well as a decrease in signal intensity for Mn in the Mn 3p region (**Figure S6**). This was expected because the XRD and SEM results showed the corrosion of $MnSb_2O_6$ during the V-t measurement. The distance of the doublet did not appear to change significantly, suggesting Mn^{2+} remained as the major Mn species at the surface.

The Sb 3d region of $MnSb_2O_6$ is shown in **Figure 7d**. The $3d_{3/2}$ peak shows a maxima at a binding energy of 540.6 eV, which is the binding energy of Sb^{5+} in Sb_2O_5, indicating the surface is Sb^{5+} in character with little to no Sb^{3+} present.[31,32] The Sb $3d_{3/2}$ peak position did not change after the V-t measurement was performed, suggesting that the oxidation state of Sb did not change during the OER. However, the intensity

decreased for both the Sb $3d_{3/2}$ peak and the Sb $3d_{5/2}$ peak, due to the loss of $MnSb_2O_6$ by dissolution, decreasing the coverage of the substrate by $MnSb_2O_6$ as shown in **Figure 6d**. The surface Mn:Sb ratio before the V-t measurement was 1:2.65, indicating an Sb rich surface. After the V-t measurement, the surface Mn:Sb ratio was 1:2.82. The fact that the surface ratio remained more or less the same, although a considerable loss of $MnSb_2O_6$ by dissolution during the V-t measurement was revealed by XRD and SEM, suggests that comparable amounts of Mn and Sb were dissolved during the V-t measurement. This could also be confirmed by the ICP-MS analysis of the electrolyte used for the V-t measurement. We observed 61.4% of the Mn and 63.9% of the Sb in the $MnSb_2O_6$ electrode were dissolved into the solution during the V-t measurement. For comparison, when we examined the electrolyte used for the V-t measurement of $CoSb_2O_6$ using ICP-MS, we found only 8.1% of the Co and 2.2% of the Sb in $CoSb_2O_6$ electrode were dissolved during the V-t measurement. We think that this level of dissolution is caused by the dissolution of amorphous or less crystalline $CoSb_2O_6$ present at the surface of nanocrystalline $CoSb_2O_6$ electrodes, which explains why we observed no changes in the XRD patterns and SEM images of $CoSb_2O_6$ before and after the V-t measurement.

Our post OER analysis shows $MnSb_2O_6$ is not stable in the long term under OER conditions in a strongly acidic medium even when it is prepared as a stoichiometric, phase pure compound. On the other hand, $CoSb_2O_6$ prepared as a stoichiometric, phase pure compound appears to be stable. This result shows that it is possible to produce an acid-stable oxide containing OER active elements such as Co. However, as we mentioned previously, the performance of $CoSb_2O_6$ and $MnSb_2O_6$ is not good enough to replace state of the art OER catalysts in acidic media.[25,28] For example, iridium oxide-based OER catalysts can achieve 10 mA/cm^2 with an overpotential of 0.20V - 0.35 V.[25,38-40]

Thus, future work will focus on the identification of oxide compositions where the atomic ratio of catalytically active metal to metal that provides a structural stability can be increased while retaining the stability of the compound in acidic media.

Activity for the CER. The recent work by Moreno-Hernandez *et al.* also suggested the possibility of using $CoSb_{2.2}O_x$ for chloride oxidation to form chlorine gas (Cl_2 (g) + $2e^- \rightleftharpoons 2Cl^-$, E^o = 1.39 V vs SHE) in a slightly acidic media (pH 2).[21] The optimum electrolyte for the chlorine evolution reaction (CER) is reported to be 4 M NaCl at pH ~2.[41,42] This combined with the anodic bias required for the CER significantly reduces the type of materials that can stably perform the CER.

In their study, $CoSb_{2.2}O_x$ was reported to be able to selectively generate 100 mA/cm^2 for chloride oxidation over 250 hours with minimal corrosion into solution.[21] $MnSb_{1.7}O_x$ also showed enhanced ability to oxidize chloride over water oxidation, however, it demonstrated significant water oxidation current before reaching 100 mA/cm^2 for chloride oxidation. Since the compounds used in this study did not have the same M:Sb stoichiometry, we wondered whether the observed difference in chloride oxidation performance was solely due to the difference in M or due to the Sb-rich and Sb-poor natures of $CoSb_{2.2}O_x$ and $MnSb_{1.7}O_x$, respectively.

Thus, we compared the CER and OER of our stoichiometric $CoSb_2O_6$ and $MnSb_2O_6$ electrodes using the conditions used by the previous study to provide a more comprehensive understanding of the composition-property relationship of the MSb_2O_6 system.

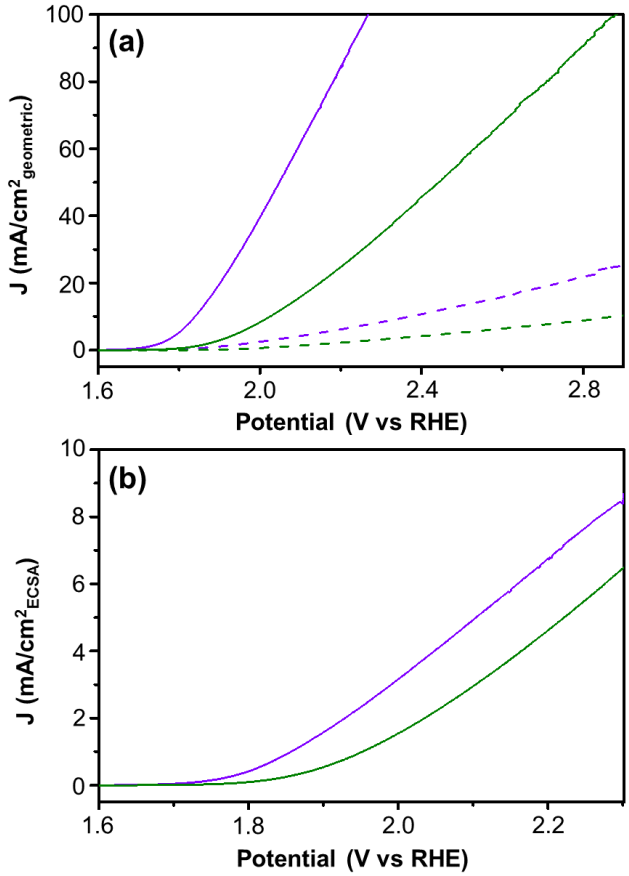

Figure 8. (a) LSVs of $CoSb_2O_6$ (purple) and $MnSb_2O_6$ (green) electrodes with the current density determined by the geometric surface area of the electrode obtained in pH 2, 4 M NaCl (solid) and in pH 2 H_2SO_4 (dashed). (b) Comparison of LSVs of $CoSb_2O_6$ (purple) and $MnSb_2O_6$ (green) with current density determined by the electrochemically active surface area.

The LSVs obtained in 4 M NaCl with the pH adjusted to 2 for chloride oxidation and pH 2 H_2SO_4 for water oxidation, respectively, are shown in **Figure 8**. Both $CoSb_2O_6$ and $MnSb_2O_6$ showed significantly enhanced activity towards chloride oxidation over water oxidation. $CoSb_2O_6$ also demonstrated an earlier onset and a higher current density than $MnSb_2O_6$ when either the geometric surface area or ECSA is used to calculate current density. This means that even when these electrodes are prepared as stoichiometric compounds, $CoSb_2O_6$ is more active for chloride oxidation than $MnSb_2O_6$. However, for our stoichiometric $CoSb_2O_6$ electrode non-negligible water oxidation occurred at potentials required to reach 100 mA/cm^2 for chloride oxidation, while water oxidation was completely suppressed

when $CoSb_{2.2}O_x$ was used to generate 100 mA/cm^2 for chloride oxidation in the previous study.[21] This is because our stoichiometric $CoSb_2O_6$ can perform water oxidation better than the Sb-rich $CoSb_{2.2}O_x$. This result suggests that the surface non-stoichiometry of the $CoSb_{2.2}O_x$ electrode is critical for making this electrode more selective for the CER.

CONCLUSION

We have developed a new electrochemical method to synthesize stoichiometric, phase pure $CoSb_2O_6$ and $MnSb_2O_6$ electrodes for investigation of their ability to oxidize water in acidic media. They showed similar activity towards water oxidation in 0.5 M H_2SO_4; $CoSb_2O_6$ showed a better performance when the same geometric area was used while $MnSb_2O_6$ showed a better performance when the electrochemically active surface area was considered. Also, both showed stable V-t performance during the OER at 10 mA/cm^2 over the course of a 24 hour V-t measurement. However, careful post OER analysis that examined changes in morphology, crystallinity, and film composition revealed that $MnSb_2O_6$ is not stable and gradually dissolves over time. On the other hand, $CoSb_2O_6$ is stable with a minimal loss of Co and Sb from the less crystalline region on the surface that did not affect the bulk crystallinity and morphology. The catalytic performance of the stoichiometric, phase pure $CoSb_2O_6$ is not sufficient to replace current state of the art IrO_x and RuO_x catalysts in acidic media. However, the study of $CoSb_2O_6$ demonstrated a possibility of producing an acid-stable ternary oxide containing a non-noble, OER active element, encouraging further development of practical acid-stable OER catalysts. We also examined the CER performance of $CoSb_2O_6$ and $MnSb_2O_6$ and found that both are more active for the CER than the OER in 4 M NaCl (pH 2), agreeing with a previous report on non-stoichiometric $CoSb_2O_6$ and $MnSb_2O_6$. However, our stoichiometric, phase pure compounds exhibited appreciable water oxidation current under

the potential required to generate 100 mA/cm^2 for the CER, indicating surface stoichiometry plays an important role in the activity towards the CER and OER.

ASSOCIATED CONTENT

Supporting Information

The Supporting Information is available free of charge on the ACS Publication website:

Nyquist plots and additional SEM images, XRD patterns, XPS spectra, and LSVs of $CoSb_2O_6$ and $MnSb_2O_6$.

AUTHOR INFORMATION

Corresponding Author

*K.-S. Choi. Email: kschoi@chem.wisc.edu

Notes

The authors declare no competing financial interest.

ACKNOWLEDGEMENTS

This work was supported by the Division of Chemical Sciences, Geosciences, and Biosciences Office of Basic Energy Sciences of the U.S. Department of Energy through Grant DE-SC0008707. XPS facilities and instrumentation used in this work were supported by the NSF through the University of Wisconsin Materials Research Science and Engineering Center through Grant DMR-1720415.

REFERENCES

1. Crabtree, G. W.; Dresselhaus, M. S., The Hydrogen Fuel Alternative. *MRS Bull.* **2011**, *33*, 421-428.

2. Formal, F. L.; Bourée, W. S.; Prévot, M. S.; Sivula, K., Challenges towards Economic Fuel Generation from Renewable Electricity: The Need for Efficient Electro-Catalysis. *Chimia* **2015**, *69*, 789-798.

3. Levene, J. I.; Mann, M. K.; Margolis, R. M.; Milbrandt, A., An analysis of hydrogen production from renewable electricity sources. *Sol. Energy* **2007**, *81*, 773-780.

4. Dau, H.; Limberg, C.; Reier, T.; Risch, M.; Roggan, S.; Strasser, P., The Mechanism of Water Oxidation: From Electrolysis via Homogeneous to Biological Catalysis. *ChemCatChem* **2010**, *2*, 724-761.

5. Man, I. C.; Su, H.-Y.; Calle-Vallejo, F.; Hansen, H. A.; Martínez, J. I.; Inoglu, N. G.; Kitchin, J.; Jaramillo, T. F.; Nørskov, J. K.; Rossmeisl, J., Universality in Oxygen Evolution Electrocatalysis on Oxide Surfaces. *ChemCatChem* **2011**, *3*, 1159-1165.

6. Jamesh, M.-I.; Sun, X., Recent progress on earth abundant electrocatalysts for oxygen evolution reaction (OER) in alkaline medium to achieve efficient water splitting – A review. *J. Power Sources* **2018**, *400*, 31-68.

7. Jung, S.; McCrory, C. C. L.; Ferrer, I. M.; Peters, J. C.; Jaramillo, T. F., Benchmarking nanoparticulate metal oxide electrocatalysts for the alkaline water oxidation reaction. *J. Mater. Chem. A* **2016**, *4*, 3068-3076.

8. Lee, Y.; Suntivich, J.; May, K. J.; Perry, E. E.; Shao-Horn, Y., Synthesis and Activities of Rutile IrO2 and RuO2 Nanoparticles for Oxygen Evolution in Acid and Alkaline Solutions. *J. Phys. Chem. Lett.* **2012**, *3*, 399-404.

9. Abbott, D. F.; Lebedev, D.; Waltar, K.; Povia, M.; Nachtegaal, M.; Fabbri, E.; Coperet, C.; Schmidt, T. J., Iridium Oxide for the Oxygen Evolution Reaction: Correlation between Particle Size, Morphology, and the Surface Hydroxo Layer from Operando XAS. *Chem. Mater.* **2016**, *28*, 6591-6604.

10. Reier, T.; Oezaslan, M.; Strasser, P., Electrocatalytic Oxygen Evolution Reaction (OER) on Ru, Ir, and Pt Catalysts: A Comparative Study of Nanoparticles and Bulk Materials. *ACS Catal.* **2012**, *2*, 1765-1772.

11. Cherevko, S.; Zeradjanin, A. R.; Topalov, A. A.; Kulyk, N.; Katsounaros, I.; Mayrhofer, K. J. J., Dissolution of Noble Metals during Oxygen Evolution in Acidic Media. *Chemcatchem* **2014**, *6*, 2219-2223.

12. Jovanovič, P.; Hodnik, N.; Ruiz-Zepeda, F.; Arčon, I.; Jozinović, B.; Zorko, M.; Bele, M.; Šala, M.; Šelih, V. S.; Hočevar, S.; Gaberšček, M., Electrochemical Dissolution of Iridium and Iridium Oxide Particles in Acidic Media: Transmission Electron Microscopy, Electrochemical Flow Cell

Coupled to Inductively Coupled Plasma Mass Spectrometry, and X-ray Absorption Spectroscopy Study. *J. Am. Chem. Soc.* **2017**, *139*, 12837-12846.

13. Hodnik, N.; Jovanovič, P.; Pavlišič, A.; Jozinović, B.; Zorko, M.; Bele, M.; Šelih, V. S.; Šala, M.; Hočevar, S.; Gaberšček, M., New Insights into Corrosion of Ruthenium and Ruthenium Oxide Nanoparticles in Acidic Media. *J. Phys. Chem. C* **2015**, *119*, 10140-10147.

14. Carmo, M.; Fritz, D. L.; Mergel, J.; Stolten, D., A comprehensive review on PEM water electrolysis. *Int. J. Hydrog. Energy* **2013**, *38*, 4901-4934.

15. Pourbaix, M., *Atlas of Electrochemical Equilibria in Aqueous Solutions.* 2 ed.; National Association of Corrosion Engineers: Houston, Texas, **1974**; p 524-532.

16. Tigau, N.; Ciupina, V.; Prodan, G., Structural, optical and electrical properties of Sb_2O_3 thin films with different thickness. *J. Optoelectron. Adv. Mater.* **2006**, *8*, 37-42.

17. Ozawa, K.; Sakka, Y.; Amano, M., Preparation and electrical conductivity of three types of antimonic acid films. *J. Mater. Res.* **1998**, *13*, 830-833.

18. Herrmann, J. M. J.; Portefaix, J. L.; Forissier, M.; Figueras, F.; Pichat, P., Electrical Behavior of Powdered Tin-Antimony Mixed-Oxide Catalysts. *J. Chem. Soc. Faraday T. 1* **1979**, *75*, 1346-1355.

19. Moreno-Hernandez, I. A.; MacFarland, C. A.; Read, C. G.; Papadantonakis, K. M.; Brunschwig, B. S.; Lewis, N. S., Crystalline nickel manganese antimonate as a stable water-oxidation catalyst in aqueous 1.0 M H_2SO_4. *Energ. Environ. Sci.* **2017**, *10*, 2103-2108.

20. Zhou, L.; Shinde, A.; Montoya, J. H.; Singh, A.; Gul, S.; Yano, J.; Ye, Y.; Crumlin, E. J.; Richter, M. H.; Cooper, J. K.; Stein, H. S.; Haber, J. A.; Persson, K. A.; Gregoire, J. M., Rutile Alloys in the Mn–Sb–O System Stabilize Mn3+ To Enable Oxygen Evolution in Strong Acid. *ACS Catal.* **2018**, *8*, 10938-10948.

21. Moreno-Hernandez, I. A.; Brunschwig, B. S.; Lewis, N. S., Crystalline nickel, cobalt, and manganese antimonates as electrocatalysts for the chlorine evolution reaction. *Energ. Environ. Sci.* **2019**, *12*, 1241-1248.

22. Wiechen, M.; Najafpour, M. M.; Allakhverdiev, S. I.; Spiccia, L., Water oxidation catalysis by manganese oxides: learning from evolution. *Energ. Environ. Sci.* **2014**, *7*, 2203-2212.

23. Takashima, T.; Hashimoto, K.; Nakamura, R., Mechanisms of pH-Dependent Activity for Water Oxidation to Molecular Oxygen by MnO_2 Electrocatalyst. *J. Am. Chem. Soc.* **2012**, *134*, 1519-1527.

24. Govindaraju, G. V.; Wheeler, G. P.; Lee, D.; Choi, K.-S., Methods for Electrochemical Synthesis and Photoelectrochemical Characterization for Photoelectrodes. *Chem. Mater.* **2017**, *29*, 355-370.

25. McCrory, C. C. L.; Jung, S.; Peters, J. C.; Jaramillo, T. F., Benchmarking Heterogeneous Electrocatalysts for the Oxygen Evolution Reaction. *J. Am. Chem. Soc.* **2013**, *135*, 16977-16987.

26. Stevens, M. B.; Enman, L. J.; Batchellor, A. S.; Cosby, M. R.; Vise, A. E.; Trang, C. D. M.; Boettcher, S. W., Measurement Techniques for the Study of Thin Film Heterogeneous Water Oxidation Electrocatalysts. *Chem. Mater.* **2017**, *29*, 120-140.

27. Kang, D.; Kim, T. W.; Kubota, S. R.; Cardiel, A. C.; Cha, H. G.; Choi, K.-S., Electrochemical Synthesis of Photoelectrodes and Catalysts for Use in Solar Water Splitting. *Chem. Rev.* **2015**, *115*, 12839-12887.

28. Hunter, B. M.; Gray, H. B.; Müller, A. M., Earth-Abundant Heterogeneous Water Oxidation Catalysts. *Chem*. *Rev*. **2016**, *116*, 14120-14136.

29. Biesinger, M. C.; Payne, B. P.; Grosvenor, A. P.; Lau, L. W. M.; Gerson, A. R.; Smart, R. S. C., Resolving surface chemical states in XPS analysis of first row transition metals, oxides and hydroxides: Cr, Mn, Fe, Co and Ni. *Appl. Surf. Sci.* **2011**, *257*, 2717-2730.

30. Foelske, A.; Strehblow, H.-H., Passivity of cobalt in borate buffer at pH 9.3 studied by x-ray photoelectron spectroscopy. *Surf. Interface Anal.* **2000**, *29*, 548-555.

31. Garbassi, F., XPS and AES study of antimony oxides. *Surf. Interface Anal.* **1980**, *2*, 165-169.

32. Izquierdo, R.; Sacher, E.; Yelon, A., X-ray photoelectron spectra of antimony oxides. *Appl. Surf. Sci.* **1989**, *40*, 175-177.

33. Nelson, A. J.; Reynolds, J. G.; Roos, J. W., Core-level satellites and outer core-level multiplet splitting in Mn model compounds. *J. Vac. Sci. Technol. A-Vac. Surf. Films* **2000**, *18*, 1072-1076.

34. Cerrato, J. M.; Hochella, M. F.; Knocke, W. R.; Dietrich, A. M.; Cromer, T. F., Use of XPS to Identify the Oxidation State of Mn in Solid Surfaces of Filtration Media Oxide Samples from Drinking Water Treatment Plants. *Environ. Sci. Technol.* **2010**, *44*, 5881-5886.

35. Galakhov, V. R.; Demeter, M.; Bartkowski, S.; Neumann, M.; Ovechkina, N. A.; Kurmaev, E. Z.; Lobachevskaya, N. I.; Mukovskii, Y. M.; Mitchell, J.; Ederer, D. L., Mn 3s exchange splitting in mixed-valence manganites. *Phys. Rev. B* **2002**, *65*, 113102.

36. Chigane, M.; Ishikawa, M., Manganese Oxide Thin Film Preparation by Potentiostatic Electrolyses and Electrochromism. *J. Electrochem. Soc.* **2000**, *147*, 2246-2251.

37. Nelson, A. J.; Reynolds, J. G.; Roos, J. W., Core-level satellites and outer core-level multiplet splitting in Mn model compounds. *J. Vac. Sci. Technol. A* **2000**, *18*, 1072-1076.

38. Pearce, P. E.; Yang, C.; Iadecola, A.; Rodriguez-Carvajal, J.; Rousse, G.; Dedryvère, R.; Abakumov, A. M.; Giaume, D.; Deschamps, M.; Tarascon, J.-M.; Grimaud. Revealing the Reactivity of the Iridium Trioxide Intermediate for the Oxygen Evolution Reaction in Acidic Media. *Chem. Mater.* **2019**, *31*, 5845-5855.

39. Jiang, H.; Ge, S.; Zhang, Y.; Dong, M.; Wu, S.; Wu, M.; Zhang, J.; Ge, R.; Gua, Z., Self-Supported Iridum Oxide Nanostructures for Electrocatalytic Water Oxidation in Acidic Media. *J. Phys. Chem. C.* **2020**, *124*, 2-8.

40. Seitz, L. C.; Dickens, C. F.; Nishio, K.; Hikita, Y.; Montoya, J.; Doyle, A.; Kirk, C.; Vojvodic, A.; Hwang, H. Y.; Norskov, J. K.; Jaramillo, T. F., A highly active and stable IrOx/SrIrO3 catalyst for the oxygen evolution reaction. *Science*. **2016**, *353*, 1011-1014.

41. Brinkmann, T.; Giner-Santonja, G.; Schorcht, F.; Roudier, S.; Delgado Sancho, L., *Best Available Techniques (BAT) Reference Document for the Production of Chlor-alkali.* **2014**. 13-17.

42. Karlsson, R. K. B.; Cornell, A. Selectivity between Oxygen and Chlorine Evolution in the Chlor-Alkali and Chlorate Processes. *Chem. Rev.* **2016**. *116*, 2982-3028.

TOC FIGURE